Applications in Energy and Combustion Science 18 (2024) 100269

Contents lists available at ScienceDirect

Applications in Energy and Combustion Science

journal homepage: www.elsevier.com/locate/jaecs

Planar laser-induced incandescence for the study of soot production in a multi-sector RQL Jet A combustor

Russell McGrath [a], Jeremiah Juergensmeyer [b], Robert Bond [b], Ezekiel Bugay [b], Shawn Wehe [b], David Wu [b], Adam Steinberg [b], Wenting Sun [b], Yi Chen Mazumdar [a,*]

[a] Woodruff School of Mechanical Engineering, 801 Ferst Dr, Atlanta, 30332, GA, United States
[b] Guggenheim School of Aerospace Engineering, 270 Ferst Dr, Atlanta, 30332, GA, United States

ARTICLE INFO

Keywords:
Aeroengine combustion
Jet A fuel
Time-resolved laser induced incandescence
Non-volatile particulate matter
Soot volume fraction
Soot incandescence decay time

ABSTRACT

Understanding the production of non-volatile particulate matter (nvPM), which is composed primarily of soot, is critical not only for reducing emissions but also for improving engine performance. While there has been significant prior work studying the fundamentals of soot formation, there is significantly less work that investigates soot formation with realistic aeroengine geometries, injectors, and fuels in high pressure conditions. In this work, soot production in a three-sector rich-quench-lean (RQL) aeroengine combustor is studied with Jet A fuel. Global equivalence ratios ranging of 0.10 to 0.20 and pressures ranging from 2.7 to 6.9 bar absolute (40 to 100 psia) are tested. In order to characterize *in-situ* soot production near the fuel injectors, two-dimensional laser-induced incandescence is utilized to estimate single-shot and average soot volume fractions. Time-resolved laser-induced incandescence is then used to create single camera and single laser-shot incandescence decay time images in order to infer how soot particle sizes evolve. Results show a significant increase in soot production at higher global equivalence ratios and higher pressures. Incandescence decay times, however, do not change significantly over the same range of conditions. These measurements can not only help understand soot distributions in practical RQL systems but also help improve future aeroengine combustor designs.

1. Introduction

Reducing the emission of non-volatile particulate matter (nvPM), which is composed primarily of soot, is critical for meeting a variety of environmental, health, and performance metrics. Aeroengine soot emissions, for example, can have long term impacts on climate [1] as well as human health [2]. When soot is created in a flame or deposited on the inside of engine surfaces, it can also enhance radiation heat transfer to various components, thereby reducing engine efficiency and lifetime. While scenarios that increase soot production, such as rich-burn conditions, may be considered sub-optimal, these conditions can also be used strategically in various practical combustor designs. Rich-burn, quick-mix, lean-burn or rich-quench-lean (RQL) combustors, for instance, utilize a fuel rich region to achieve improved combustion stability, lower flame temperatures, and decreased nitrogen concentrations, reducing the production of NOx [3,4]. Because of this trade off, understanding soot distributions in these combustors is critical for improving aeroengine designs and minimizing nvPM production.

Fundamental soot production has been extensively studied in various laboratory environments. Existing work includes studies using simple flow geometries such as counterflow flames [5,6], turbulent premixed flames [7,8], shock tubes [9], laminar premixed flames [10], and laminar diffusion jet flames [11–14]. In most cases, ethylene or methane are used for these studies. Simple combustor geometries [15–17] and high pressures up to 32 bar in counterflow flames [5] and 100 bar in diffusion flames [11] have also been studied in the literature. Despite the extensive body of work, the chemical kinetics of soot formation and oxidation [18,19] are still difficult to model. Recently, several studies have also been conducted in more realistic engine geometries utilizing simple fuels like ethylene, methane, and kerosene [6,20–23] and simple jet-in-crossflow injector geometries [24]. Comparisons between Jet A fuels and more laser-diagnostic-friendly fuels, such as Testbenzin D80, have also been investigated using realistic combustor geometries [25]. Extensive studies with Jet A fuels in complex injector configurations [26–28] have been investigated, but these experiments have focused on lean premixed combustors. While these studies provide a lot of insight into soot production, changing the fuel type, mixing scheme, or injector geometry can significantly alter soot production

* Corresponding author.
E-mail address: ellen.mazumdar@gatech.edu (Y.C. Mazumdar).

https://doi.org/10.1016/j.jaecs.2024.100269
Received 11 November 2023; Received in revised form 26 February 2024; Accepted 23 April 2024
Available online 30 April 2024

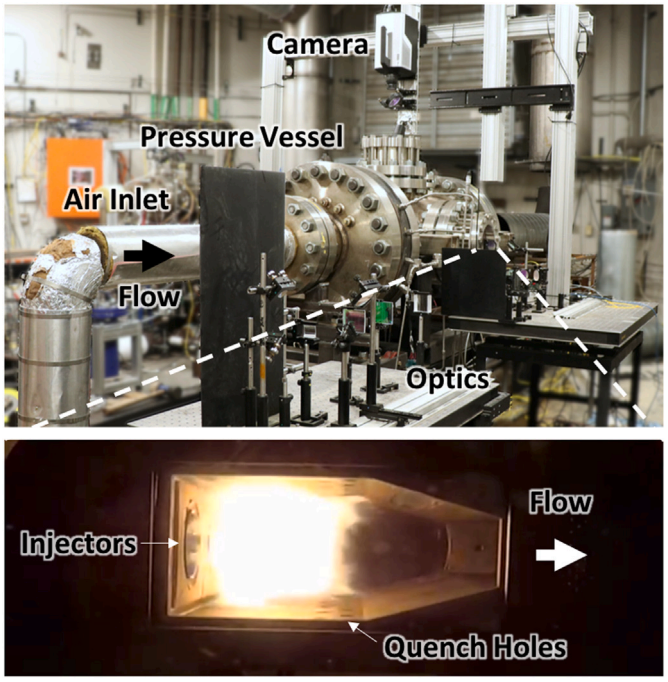

Fig. 1. Experimental setup is described showing the pressure vessel for the combustor, air inlet, optics, and high speed camera. An image of the flame, injectors, and quench holes is also shown from a side window.

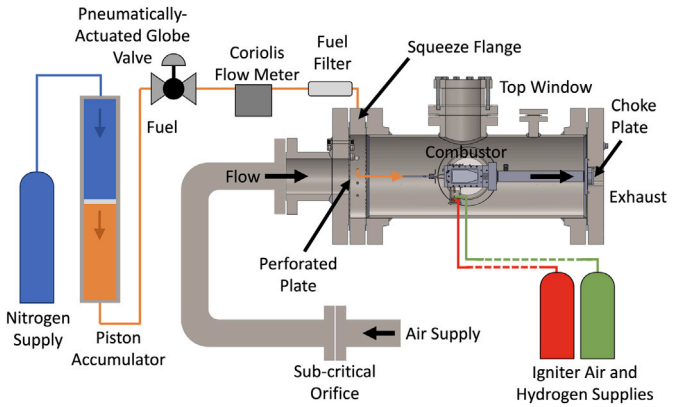

Fig. 2. Side view of pressure vessel shows the process flow, instrumentation, and control elements for the combustor.

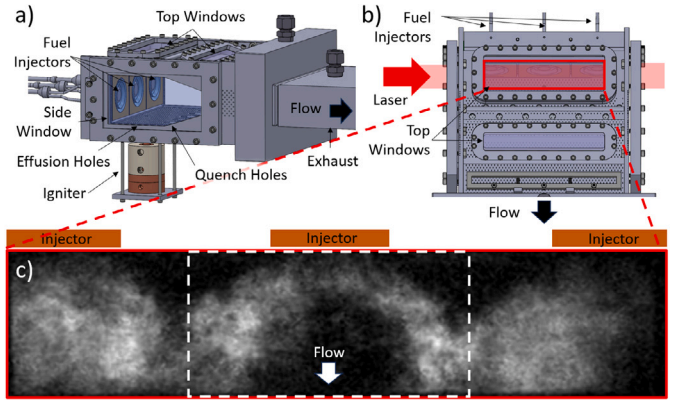

Fig. 3. (a) Side view of combustor illustrates the hydrogen torch ignitor, fuel injectors, effusion cooling holes, quench holes, and windows. (b) Top view of combustor highlights the laser path and top window used for imaging. (c) Chemiluminescence image of flame shows the spray cones for all three injectors. The white box highlights the area used for detailed comparisons.

and oxidation [20,23]. Thus, more studies that investigate *in-situ* soot production for realistic combustors, injectors, and fuels are needed.

In this work, we apply two-dimensional (2D) or planar laser-induced incandescence (LII) and incandescence decay time measurements for the first time in a three-sector RQL combustor utilizing swirl injectors and Jet A fuel. First, the experimental setup (shown in Fig. 1) detailing the pressure vessel design, RQL combustor, and control systems are described. Next, the LII diagnostic setup and LII models used for calibration are reported. Here, a 10 MHz high speed camera is used to capture the prompt LII signal intensity as well as the signal decay as a function of time [8]. Thus, simultaneous estimates of soot volume fraction and soot incandescence decay times can be obtained. Finally, experimental data is described for global equivalence ratios ranging from 0.1 to 0.2 and pressures ranging from 2.7 to 6.9 bar absolute (40 to 100 psia). Using these results, it is possible to understand the conditions that control soot distributions inside a realistic RQL aeroengine combustors.

2. Materials and methods

2.1. Pressure vessel and combustor design

In this work, a large stainless steel pressure vessel (rated for a maximum of 30 bar at 727 K) is utilized to contain the combustor, fuel lines, and exhaust, as illustrated in Fig. 2. The vessel has an internal diameter of 43 cm (18 in) with three 25.4 cm diameter (20.3 cm is transparent) by 10.1 cm thick fused quartz windows for optical access, one on each side for laser access and one on top for camera access. A squeeze flange mounted on the upstream side is used to pass fuel and instrumentation lines into the vessel, enabling measurement of vessel pressure and temperature at various locations along the combustor.

Air for the experiments is supplied to the system by the high pressure air supply at the Ben T. Zinn Combustion Laboratory at Georgia Tech - a blowdown system capable of supplying a stable, static pressure of up to 50 bar at 1100 K. The air flows through a sub-critical orifice used for measuring and monitoring mass flow rate, after which it enters the vessel through a perforated plate. Air then enters the combustor through the swirlers, providing the majority of the air for the rich-burn region, as well as through effusion cooling and quench holes. The distribution of air is described in more detail in the Appendix.

Fuel for this system is supplied through a 38 L (10 gal) piston accumulator, driven by a cylinder of pressurized nitrogen gas. The fuel flows through a remotely-operated pneumatic globe valve, which is used for flow control, followed by a Bronkhurst Coriolis flow meter (Cori-Flow M55, accuracy 0.2% of rate), which monitors and measures the fuel mass flow rate. Then, fuel passes through the squeeze flange into a manifold, where it is supplied evenly to all three injectors. The variation between the injectors is <4% based on liquid volume accumulation measurements taken at a variety of injection pressures.

The combustion liner for this system includes a proprietary dome face assembly with three aircraft fuel injectors and swirlers provided by Honeywell International Inc. This design represents multiple sectors of an aeroengine combustor, as illustrated in Fig. 3. The combustion liner has four fused quartz windows for optical access. Two windows on opposing sides enable laser access across all three injectors, while two windows on top provide visual access to the rich-burn and lean-burn regions. The combustion liner is made from 3D-printed Inconel 718 with small, angled effusion cooling holes covering all surfaces, both for cooling the combustor walls and for preventing soot from depositing on the walls and windows. Larger quench holes are also located on the top and bottom of the liner to enable the introduction of air downstream of the rich-burn region. Additional detailed dimension for the combustor,

windows, effusion holes, and quench holes as well as detailed air splits are described in the Appendix.

Initial combustor ignition is achieved via a hydrogen torch igniter mounted to the bottom of the combustor. Here, hydrogen and high pressure air are supplied to the igniter from pressurized cylinders outside the vessel. Opposing jets of hydrogen and air impinge on a glow plug inside the body of the ignitor, causing an internal flame. After sufficiently heating the tip of the ignitor, the air supply is closed off, causing an external diffusion flame to appear through a small hole in the bottom plate of the combustor. Jet A supply can then be slowly increased at the main injectors until a stable flame is achieved, after which the supply of hydrogen to the igniter is closed.

After the combustion gases exit the liner, the combustion products are exhausted out of the back of the pressure vessel through a water-cooled exhaust system mounted to the downstream flange, which also acts as the primary support for the combustor. Choke plates of varying size (23 mm in height and 60 to 75 mm in width) are attached to the exhaust outlet to achieve a desired differential pressure across the combustion liner walls to help ensure proper droplet breakup. During experiments, the desired temperature and pressure are first set from the building supply and the vessel is preheated to the desired temperature range. Then, the air supply is increased until the stagnation pressure in the vessel, P_3, reaches the desired test point. Then, a custom LabView program (run from an adjacent control room) is used to ignite the hydrogen torch, adjust valves, monitor temperature/pressure sensors, control lasers, and collect diagnostic data. The LabView program is also used to adjust fuel flow rates until the desired equivalence ratio is reached. Due to the presence of the fixed-size choke plate at the exit of the combustor, the mass flow rate cannot be independently controlled during a run. Thus, changing the pressure requires adjusting the global equivalence ratio (and vice versa) until both variables reach the desired values. After the transient effects subside after each adjustment, data are collected. Due to building pressure tank limitations, data collection is typically limited to approximately an hour per run. To conserve resources, a limited number of data sets are collected at each condition and several test conditions are explored following a single ignition.

For these experiments, the target inlet pressure conditions P_3 range from 2.7 to 6.9 bar absolute (40 to 100 psia), the target global equivalence ratios ϕ range from 0.10 to 0.20, the inlet temperatures T_3 range from 470 to 640 K, and the pressure drop across the liner compared to the inlet pressure dP/P_3 is typically 3.4%. Note that all pressures in this paper are listed as absolute pressures and all experiments are conducted at an ambient room pressure of 1 bar. Additionally, note that this paper quotes global equivalence ratios. Local equivalence ratios can be estimated by using the air split data described in the Appendix. For these experiments, the dome face air split is 18%, which gives local equivalence ratios of 0.55 to 1.1 in the rich-burn region for the corresponding global equivalence ratio range of 0.1 to 0.20. The test conditions used for this paper are selected from a full list of realistic combustor operating conditions and are chosen based on facility constraints, risk of damage to components, and optical diagnostic data quality. A full list of target test conditions and their corresponding measured pressures, global equivalence ratios, air inlet temperatures, and air and fuel mass flow rates are tabulated in the Appendix.

2.2. LII diagnostic

For the LII optical diagnostics, a Spectra-Physics Quanta-Ray Pro-250 Nd:YAG laser is used to generate a 1064 nm beam at a frequency of 10 Hz (pulse-to-pulse energy variation <3%). The layout for the optical elements in the diagnostic is shown in Fig. 4. Here, vertical expansion of the beam is achieved using lenses L1 and L2 (concave and convex cylindrical lenses with focal distances of −50 mm and 300 mm, respectively). Afterwards, the beam is horizontally compressed using cylindrical lenses L3 and L4 (focal distances of 250 mm and −50 mm, respectively). The final beam dimension of 28 × 1.22 mm at a knife gate

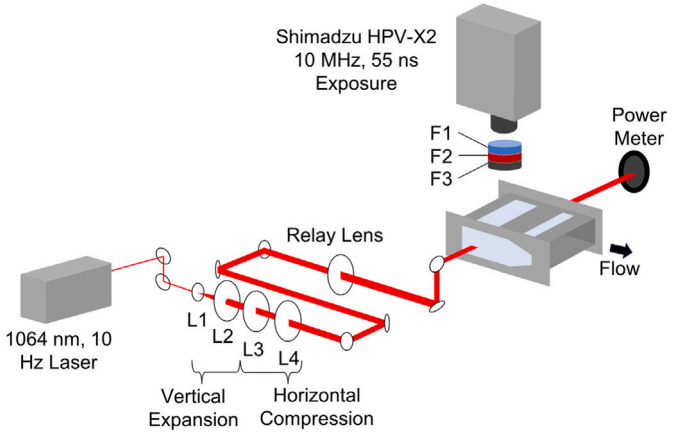

Fig. 4. Layout of optical setup for the LII diagnostics are illustrated. L1 - concave cylindrical lens $f = -50$ mm, L2 - convex cylindrical lens $f = 300$ mm, L3 - convex cylindrical lens $f = 250$ mm, L4 - concave cylindrical lens with $f = -50$ mm, F1 - 640 nm bandpass filter with 75 nm FWHM, F2 - 1064 nm notch filter with 73 nm FWHM, F3 - neutral density filter OD 0.3.

is then relay imaged into the center of the combustor using a 500 mm focal distance cylindrical lens positioned two focal lengths from the centerline of the combustor. This long focal-length relay lens keeps diffraction patterns to a minimum (ripple <1%) while keeping beam expansion due to diffraction low (<9.6% deviation in beam FWHM from the center to either edge of the camera field-of-view). Because the laser sheet passes through the center of all three fuel injectors, a larger sheet thickness is used to maximize sheet uniformity. Thus, analysis of turbulent features is not conducted on the measured LII data. Next, the laser intensity is measured on the far side of the combustor using a Thorlabs S350C thermopile power meter with a 200 Hz sampling rate and 40 mm active detector diameter. Due to the large size of the detector, the entire beam could be successfully captured even if some beam steering occurs. These average power measurements are later used to calibrate volume fraction measurements.

The LII signal is imaged from above the pressure vessel using a Shimadzu HPV-X2 high speed camera (250 × 400 pixels, 32 μm pixels, additional dynamics can be found in [29]) with a 50 mm, f/1.8 lens (depth of field >12 mm). This results in an X and Y spatial resolution of 0.46 mm per pixel. Due to the large spatial resolution values, spatial averaging within each pixel that biases towards higher temperatures, volume fractions, and decay times is expected. For this work, images are collected at a rate of 10 MHz in the zig-zag interpolation mode with an exposure time of 55 ns. In this mode, the camera captures a burst of 256 images (total capture time of 25.6 μs, excess frames are not used) during which the flow dynamics are essentially frozen. This data takes approximately 10 s to download before the camera can capture images again. The 10 MHz high speed burst mode capability is ideal for capturing single-laser-pulse incandescence decay with a low repetition rate laser, but is not ideal for studying turbulence dynamics in soot, which can be investigated with other LII techniques [30]. To condition the signal for this camera, a 1064 nm notch filter (73 nm full-width at half-maximum, FWHM) is used to reduce scattering and reflections from the laser and a 640 nm bandpass filter (75 nm FWHM) [8,31] is used to attenuate signal from chemiluminescence and Swan band emissions while maximizing the measured LII signal. Finally, an OD 0.3 neutral density filter is used to slightly adjust the LII signal intensity to within the camera dynamic range.

Both the camera and laser are operated using a timing box to ensure consistent and precise capture of the prompt LII signal (capture starting at t = 0 ns with laser arrival and integrated for 55 ns). In this work, the camera acquires a total of 256 back-to-back frames, capturing the prompt LII signal, LII signal decay, and background chemiluminescence

within in a single video. A subset of background images are averaged and then subtracted from the prompt and decay images to isolate the incandescence signal [26,31,32]. At each temperature and pressure condition, at least 25 data sets are collected at 10 s intervals for a total of 4 min. Since the global flow residence times are typically on the order of 5 ms based on chemiluminescence videos, each shot is uncorrelated, enabling both instantaneous and average LII data to be analyzed.

3. Theory

3.1. Volume fraction model

The soot volume fraction inside a flame is estimated by measuring the intensity of incandescence emitted by soot as it is quickly heated by a high-powered laser pulse [33,34]. To estimate the volume fraction, the laser power absorbed by soot is related to the LII signal observed by the camera. For this, the Beer–Lambert-Bouguer law is used,

$$\frac{I_{FL}-I_{FO}}{I_{OL}-I_{OO}} = exp\left(\frac{-Kef_vL}{\lambda}\right), \tag{1}$$

where I_{FO} indicates a power measurement with only the flame present, I_{OL} indicates a power measurement with only the laser present, I_{FL} indicates a measurement with both flame and laser present, and I_{OO} indicates a measurement taken in absence of both laser and flame. I_{FO} and I_{OO} are used to subtract thermal effects from the flame and pressure vessel from power measurements I_{FL} and I_{LO}, effectively isolating the effects of soot absorption on the incident laser power. Ke is a dimensionless extinction coefficient (Ke = 5.01 at 1064 nm [35–37]), which is based on the soot absorption function, laser wavelength, fuel type, and other factors [38–40]. In these equations, L is the path length of the laser in the flame, λ is the laser wavelength, and f_v is the line-averaged soot volume fraction. The line-integrated soot volume fraction (approximated as f_vL) can be related to the line-integrated laser-induced incandescence signal (approximated as $CS_{LII}L$) using,

$$f_vL \approx \int f_v dl = C\int S_{LII}dl \approx CS_{LII}L \tag{2}$$

where S_{LII} is the LII signal of each pixel, and C is the calibration constant. Rearranging Eq. (1) yields,

$$f_vL = \frac{-\lambda}{Ke} ln\left(\frac{I_{FL}-I_{FO}}{I_{OL}-I_{OO}}\right). \tag{3}$$

As all terms on the right hand side are known, the calibration constant can be solved as,

$$C \approx \frac{f_vL}{\int S_{LII}dl}, \tag{4}$$

which can then be applied to calculate the average volume fraction per pixel along each row of the image,

$$f_v \approx CS_{LII}. \tag{5}$$

By combining data from all the rows, the soot volume fraction for an entire image can be estimated. To reduce the dependence of incandescence intensity on laser power and to enable more accurate calibration, high laser fluences are needed to saturate the incandescence output via soot sublimation.

3.2. Soot incandescence decay time model

Time-Resolved LII (TiRe-LII) can be used to infer information on soot particle and agglomerate sizes based on the decay time of the LII signal [41]. Currently, several different 2D TiRe-LII techniques exist for capturing turbulent flames [7,42–44], but these techniques require the use of multiple cameras. To perform 2D TiRe-LII in this work, a planar laser sheet is passed through an area of interest and a series of images are used to capture the prompt LII signal as well as the decay of the signal over several frames at 10 MHz using a single camera and single laser shot method [8,31]. Heat transfer models for soot agglomerates [41,45] can be used to extract information. Accurate estimates of soot particle or agglomerate size, however, are difficult to obtain without calibration against soot sampling data or accurate parameter estimates (i.e. local bath gas temperature, number of primary particles per soot aggregate). Thus, this work focuses on estimating incandescence decay times, which can be used to infer but not quantitatively determine particle and agglomerate sizes.

A simplified soot TiRe-LII model, however, can provide insight on how parameters like pressure can affect soot particle size and incandescence decay times. For this model, conservation of energy can be used around the soot agglomerate,

$$\frac{dU_{Internal}}{dt} = \dot{Q}_{Absorp} - \dot{Q}_{Rad} - \dot{Q}_{Cond} - \dot{Q}_{Sub}, \tag{6}$$

where $\dot{Q}_{Absorp}$ is energy absorbed from the laser, $\dot{Q}_{Rad}$ is heat loss due to radiation, $\dot{Q}_{Cond}$ is heat loss due to conduction, and $\dot{Q}_{Sub}$ is heat loss due to sublimation. For the Liu model [45],

$$\frac{dU_{Internal}}{dt} = \frac{\pi}{6}d^3N_p\rho_sc_s\frac{dT}{dt}, \tag{7}$$

$$\dot{Q}_{Absorp} = \frac{\pi^2d^3E(m)F_0q(t)N_p}{\lambda}, \tag{8}$$

$$\dot{Q}_{Rad} = N_p\int_0^\infty \frac{8\pi^3c^2h}{\lambda^6}\frac{d^3E(m)}{exp(hc/k_B\lambda T)-1}d\lambda, \tag{9}$$

$$\dot{Q}_{Cond} = \alpha\pi R_a^2\frac{p_g}{2}\sqrt{\frac{8k_BT_\delta}{\pi m_g}}\frac{\gamma^*+1}{\gamma^*-1}\left(\frac{T}{T_\delta}-1\right). \tag{10}$$

Here, d is the soot primary particle size, N_p is the number of primary particles per soot aggregate, ρ_s is the density of soot, c_s is the specific heat of soot, $E(m)$ is the soot absorption function (0.3 for Jet A which is similar to kerosene [46]), F_0 is the laser fluence, $q(t)$ is the laser temporal profile function (characterized with a fast photodiode), λ is the wavelength of the laser, and T is the temperature. The constants h, k_B, and c are the Planck constant, Boltzmann constant, and speed of light, respectively. The values of these parameters for Jet A fuel can be found in our prior work [31]. For short laser pulse durations and significantly longer camera integration times, the detailed laser temporal profile is not expected to have a measurable effect on the incandescence decay profiles captured by the camera. Note that for this model, it is not possible to independently estimate the d and N_p because of their close coupling. Thus, one of these two quantities must be measured in order to calculate the other.

The Fuchs method [47–49] can be utilized to estimate conduction, where a limiting sphere is constructed with conduction in the free-molecular regime assumed inside the sphere, and conduction in the continuum regime assumed outside the sphere. For the free-molecular regime conduction term, which is closer to the particle, p_g is the ambient pressure, m_g is the mass of one of the surrounding gas molecules, α is the thermal accommodation coefficient for soot, R_a is an equivalent sphere radius calculated based on the aggregate projected area, and γ^* is an average specific heat ratio. The size of the limiting sphere boundary layer thickness δ and the temperature at the limiting sphere T_δ can be solved iterative with conduction that occurs outside the limiting sphere [45].

To convert these equations to incandescence decay profiles, the temperature as a function of time is first determined. Then, the temperature profiles are converted to optical incandescence profiles by assuming grey body emission for different wavelengths, applying Planck's law, and using the emissivity coefficients for soot. For lower laser fluences, conduction mechanisms dominate over radiation mechanisms, producing an exponential decay of incandescence intensity as a function time. Larger particles and agglomerates tend to have longer decay time constant while smaller particles and agglomerates tend to have shorter decay time constants.

For the higher laser fluences used to estimate soot volume fraction, sublimation can begin to play an important role. This can be modeled as [41],

$$\dot{Q}_{Sub} = -\frac{\Delta H_v N_p}{W_v}\frac{dM}{dt}, \tag{11}$$

$$\frac{dM}{dt} = -\frac{\pi d^2 W_v \alpha_m p_v}{R_p T}\left(\frac{R_m T}{2W_v}\right)^{1/2}, \tag{12}$$

$$d = \left(\frac{6M}{\pi \rho_s}\right)^{1/3}. \tag{13}$$

Here, M is the mass lost via sublimation per soot particle in the agglomerate, ΔH_v is the enthalpy of formation of sublimed carbon, W_v is the molecular weight of the sublimed carbon, α_m is the mass accommodation coefficient, p_v is the partial pressure of sublimed carbon, R_p is the universal gas constant in effective pressure units, and R_m are the universal gas constant in effective mass units.

Typically, sublimation occurs in the short time period during and slightly after laser incidence. Once particles cool, conduction once again dominates the incandescence decay times. Using the model described above, the effect of sublimation on the time constants measured by the camera can be assessed. Results at fluences of 0.30 J/cm^2, which is just above the sublimation threshold, show that the presence of sublimation in the LII signal contributes to a <1.6% bias on camera measurements of the decay time constant. Operating in the sublimation regime also causes particles to decrease in size. However, for fluences just above the sublimation threshold, the particle sizes do not change significantly. TiRe-LII simulations show that sublimated particles would shrink by <2%, which would lead to a small left-to-right asymmetry. While sublimation can be modeled, there are still significant uncertainties and validation challenges. Thus, fully understanding the effects of sublimation is still an active area of research [41]. Overall, while sublimation can alter particle sizes and decay time constants, larger particles should still take longer to decay than smaller particles. Thus, even with sublimation, this model can be used to understand how flame parameters can be related to incandescence decay times and can be used to infer relative soot particle sizes for a given 2D image. Additionally, based on the model formulation and additional simulations of flame conditions, comparisons across equivalence ratios at a fixed pressure can be conducted. Multiplying the time constants by the pressure values (see Eq. (10)) can further allow rough comparisons of relative soot particle and agglomerate sizes across pressures.

4. Results and discussion

4.1. Calibration

Prior to performing soot volume fraction measurements, the laser power necessary for sublimating the soot must first be determined. For this experiment, the flame is turned off and laser power levels are set using an attenuator (half-wave plate and polarizing beam-splitter) to dump excess power and reach the desired laser fluence. Then, the combustor is ignited and 15 measurements are taken at each laser fluence level inside the turbulent Jet A flame. The signal intensity of each image is averaged and the standard deviation is calculated. Laser saturation curves are then captured at multiple conditions. An example for a constant pressure of 4.1 bar absolute (60 psia) with an equivalence ratio of 0.15 is shown in Fig. 5. For this figure, the LII signal saturation occurs at or below a threshold of 0.24 J/cm^2. Therefore, a fluence of 0.30 J/cm^2, which is above the sublimation threshold, is used for experiments at different test conditions. Additionally, as discussed in Section 3.2, since the relative rank of decay time constants and inferred relative particle sizes do not change with laser fluence, this work prioritizes measurements of the quantitative volume fraction. Thus, higher laser fluences above the sublimation threshold are used in this study for both types of measurements.

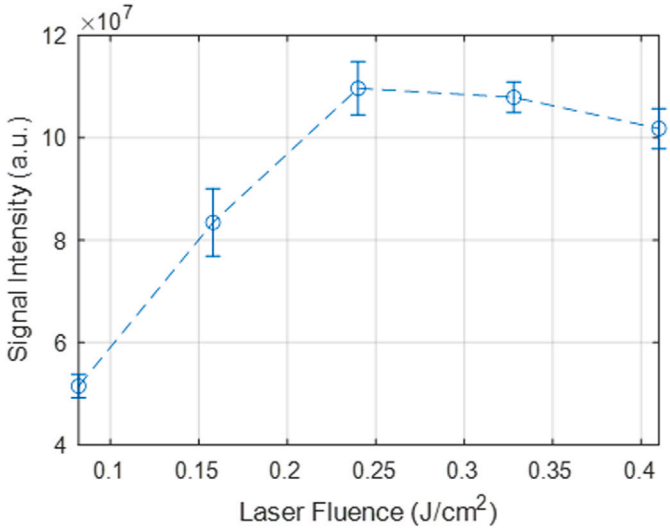

Fig. 5. Average LII signal intensity at various excitation fluences is described for a test case at 4.1 bar (60 psia) pressure and 0.15 global equivalence ratio. The signal saturation is estimated in this experiment to occur at 0.24 J/cm^2. Error bars indicate the standard deviation of 15 measurements at each laser fluence.

After determining the saturation curves, the calibration coefficient C for soot volume fraction estimation is found. To calculate the coefficient, several turbulent flame conditions are tested at different pressures and equivalence ratios (11 different conditions, with 169 laser shots). First, I_{OO} and I_{OL} are measured. Then, the combustor is ignited and taken to condition before I_{FO} is measured. Then, the I_{FL} data is taken at the same time as the Shimadzu camera data. Because the combustor width is larger than the top window, an additional LII signal compensation factor of 20% ± 3.5% is added to the calibration based on data from experimental measurements as well as computational fluid dynamics (CFD) simulations that span the range of conditions tested in this work. Both these methods show little to no soot production near the side windows due to the presence of window cooling air. In these calibrations, uncertainties from intensity measurements are propagated through Eqs. (3) and (4). Variations in intensity measurements during a single condition over several minutes tend to be low (1.2%), while the variations in intensity measurements from calibration-to-calibration and day-to-day are much higher, dominating the uncertainty. Altogether, the experimental results show no correlation between the C constant and the pressure or equivalence ratio. Additionally, the laser wavelength, fuel type, camera settings, and other parameters do not change between experiments. Therefore, the calibration coefficients are calculated and averaged together, which helps increases the sample size and reduce the standard error. The resulting calibration coefficient is found to be $C = 7.01 \times 10^{-11} \pm 1.20 \times 10^{-11}$ (standard error) parts per arbitrary intensity unit.

4.2. Soot volume fraction

Fig. 6 shows a subset of volume fraction data collected with a constant global equivalence ratio ϕ of 0.12. The images show pressures of 4.1, 4.8, 5.5, 6.2, and 6.9 bar absolute (60, 70, 80, 90, and 100 psia) with flow direction from top to bottom and laser propagation from left to right. Measurement at 2.7 and 3.4 bar absolute (40 and 50 psia) also contained soot, but are omitted for clarity. Here, the X coordinate is centered on the center fuel injector and the Y coordinate is zero at the dome face. Fig. 6a shows soot volume fraction measurements for individual laser and camera shots at each condition, while Fig. 6b shows average soot volume fraction from 25 data sets at each condition. The measurement uncertainty for these experiments is 17% (standard error), which is dominated by the uncertainty from the calibration

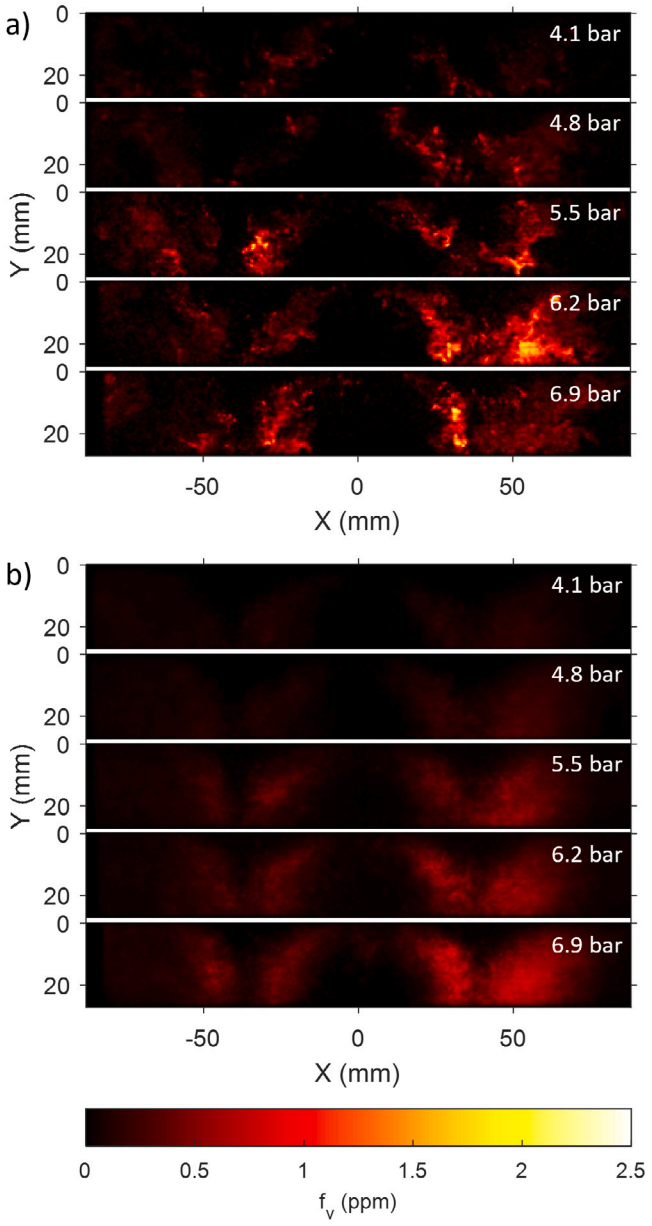

Fig. 6. Volume fraction data is illustrated for an equivalence ratio of 0.12 at pressures of 4.1, 4.8, 5.5, 6.2, and 6.9 bar absolute. The laser beam passes through the combustor from left to right. (a) Single-shot volume fraction images and (b) average (of 25 images) volume fraction images are shown.

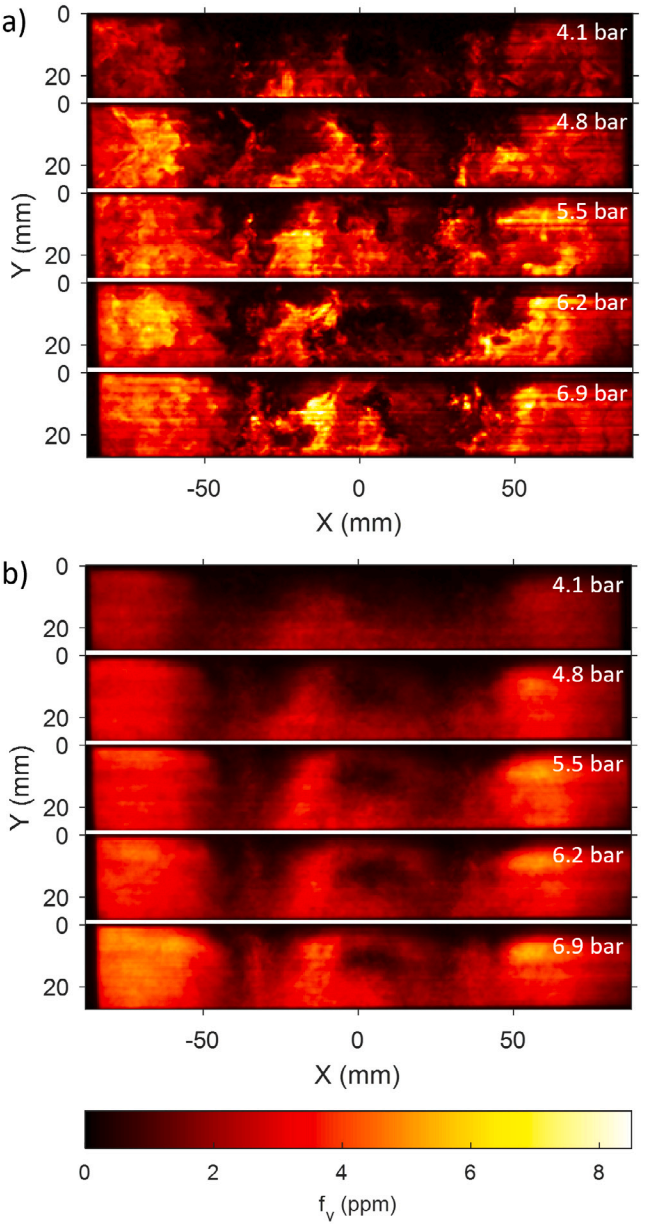

Fig. 7. Volume fraction data is illustrated for an equivalence ratio of 0.20 at pressures of 4.1, 4.8, 5.5, 6.2, and 6.9 bar absolute. The laser beam passes through the combustor from left to right. (a) Single-shot volume fraction images and (b) average (of 25 images) volume fraction images are shown.

constant, as discussed in Section 4.1. The instantaneous images demonstrate clear turbulent flame features with concentrated areas of soot appearing to vary from shot-to-shot. These hot spots, which produce soot volume fractions that are 3 × higher than the maximum values found in the average volume fraction data, can potentially be due to higher local instantaneous equivalence ratios or variations in local mixing with ambient air. The average volume fraction images, on the other hand, are more uniform, suggesting that the hot spots in soot production average out over time. In these images, there does not appear to be soot in the recirculation zones between the swirl injectors. Overall, there is significant variation in soot volume fractions from shot-to-shot, but average soot production is typically <2 ppm.

Fig. 7 shows similar images of volume fraction measurements made at a constant global equivalence ratio of 0.20. The images are taken at pressures of 4.1, 4.8, 5.5, 6.2, and 6.9 bar absolute. Measurement at 2.7 and 3.4 bar are also obtained but are omitted for clarity. Similar to the prior dataset, Fig. 7a shows instantaneous soot concentrations with more apparent turbulent flame features, while Fig. 7b shows average images with more uniform distributions. In this dataset, increased recirculation of soot appears and is especially visible at pressures above 4.8 bar. In the higher pressure cases, identifiable columns of soot appear around X = 40 and −40 mm between the injectors. Data from high speed chemiluminescence videos, which are taken with the existing Shimadzu camera setup at a lower frame rate, clearly shows how these columns of soot move into and out of the page. For this higher equivalence ratio, soot production is significantly higher. However, because the fluences above the sublimation threshold are used for this work, the effects of laser attenuation are reduced. For most cases at lower global equivalence ratios, losses due to attenuation, sublimation, and scattering are measured to be small. For the highest

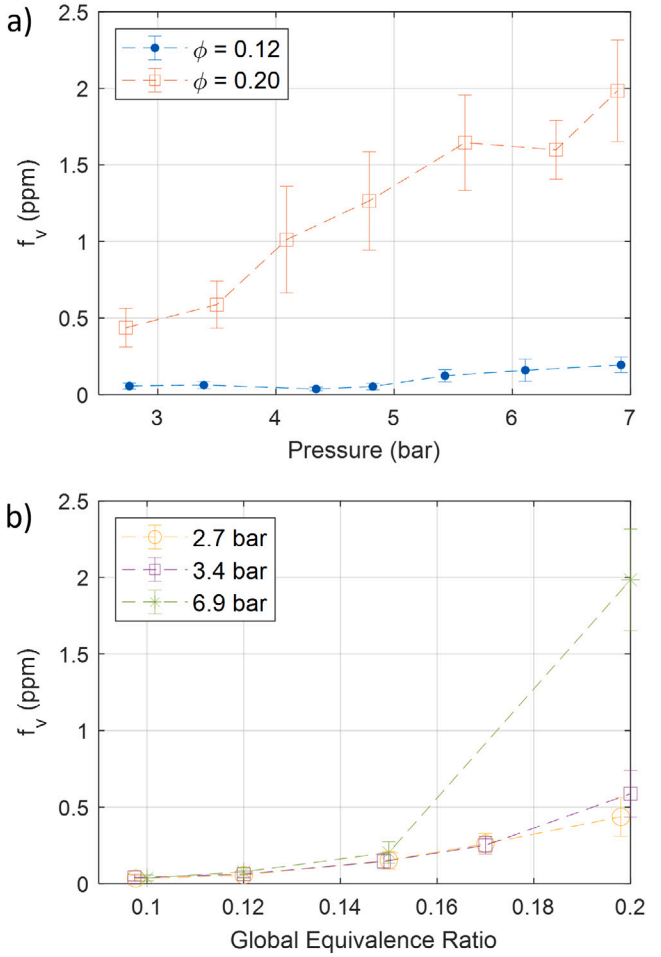

Fig. 8. Average volume fraction near the center injector region-of-interest (highlighted in white in Fig. 3c) at (a) a constant global equivalence ratio and at (b) a constant pressure are illustrated. Error bars are determined by calculating the standard error of the mean within the region-of-interest from the average volume fraction images.

average volume fraction case in Fig. 7b at 6.9 bar and $\phi = 0.20$, a left-to-right attenuation of 10% is observed in the volume fraction data.

Compared to the spray cones visible in the 0.12 global equivalence ratio cases, the soot profiles for the side injectors for the 0.20 global equivalence ratio cases appear to have a different pattern than the soot profile from the center injector. Here, the soot volume fraction for the center injector appears to have a small hole in the center where little to no soot is present. Based on additional flow tests and combustor CFD simulations, this feature is determined to be due to the geometry of the three-injector system. Since the center injector does not interact with the side walls and has recirculation zones on either side, the flow structure creates a center portion that has a lower density of soot. Overall, the center injector has the lowest contribution from side-wall cooling effects, has the best optical access, and is most likely to match the performance of injectors in a full annular assembly. Thus, additional analysis is conducted using data from the area around the spray cone of the center injector.

Fig. 8 shows the average volume fraction compiled over a series of experiments for the spray region near the center injector, as highlighted in Fig. 3c. Fig. 8a shows varying pressure conditions at a constant global equivalence ratio while Fig. 8b shows varying global equivalence ratios at different vessel pressures. In Fig. 8a, there is a clear increase in soot production from $\phi = 0.12$ to $\phi = 0.20$, indicating a strong dependency between soot production and the global equivalence ratio. Note that

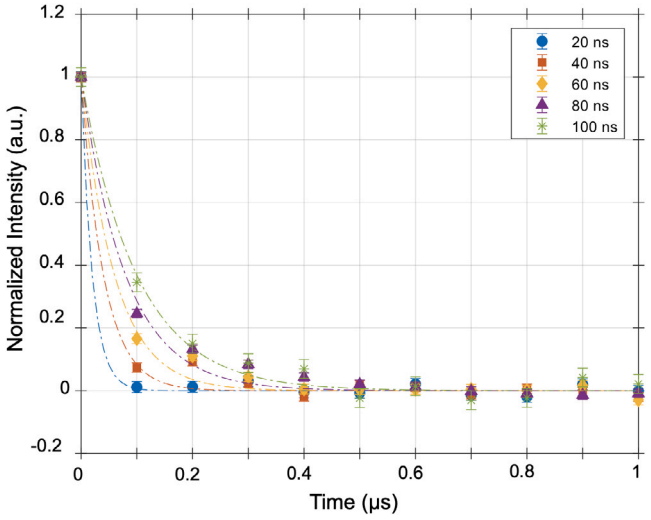

Fig. 9. Various time constant fits are shown for incandescence decays captured on selected pixels at a condition of 2.7 bar and 0.20 global equivalence ratio. Error bars show the standard deviation from camera noise, which comes from the background removal and normalization process.

local equivalence ratios in the rich-burn region are significantly higher than global values. The 0.12 equivalence ratio conditions show a small increase in the absolute soot volume fraction with pressure, going from 0.06 ± 0.02 ppm at 2.7 bar to 0.19 ± 0.05 ppm at 6.9 bar. By comparison, the 0.20 equivalence ratio conditions show a larger increase in the absolute volume fraction, going from 0.44 ± 0.13 ppm at 2.7 bar to 1.98 ± 0.33 ppm at 6.9 bar. The proportional increase for these two cases, however, is similar with the 0.12 case producing a 3.2× and the 0.20 case producing a 4.5× increase in soot volume fraction with pressure increasing from 2.7 to 6.9 bar.

Fig. 8b further illustrates trends related to global equivalence ratio and pressure. Mean volume fraction near the center injector for the 6.9 versus the 2.7 bar conditions is 0.003 ppm higher at a global equivalence ratio of 0.10, 0.05 ppm higher at a global equivalence ratio of 0.15, and 1.55 ppm higher at a global equivalence ratio of 0.20. This data indicates that the sensitivity of soot production to the global equivalence ratio is highest for the higher pressure conditions tested in this work, which go up to 6.9 bar.

Part of this increase in soot volume fraction near the area of interest can likely be attributed to lack of soot in the recirculation zones at the low pressure and low equivalence ratio conditions, as in the 2.7 bar, 0.10 and 0.12 equivalence ratio cases. At higher global equivalence ratios, where soot does not completely oxidize before recirculation, vessel pressure would have a greater influence on volume fraction in the area of interest by driving soot back up into the rich-burn zone between the injectors. Another major contributing factor to this effect is an increase in the speed of the combustion reactions at higher pressures, which would also result in higher soot concentrations [50,51].

4.3. Soot incandescence decay time distributions

In order to infer the effects of relative particle size, time constant fits to the incandescence decay profiles must first be computed. To process this data, background chemiluminescence from five images taken after incandescence decay (1.6 to 2.0 μs after laser arrival) are averaged and subtracted from the LII images. Then, the data series from a single laser and camera shot is normalized against the prompt LII frame to speed up the fitting procedure. Finally, exponential decay curves are fit to each pixel in the data series to estimate decay time constants. Fig. 9 shows the time constant fits and associated uncertainty from the background removal and normalization process for five different pixels, each with a

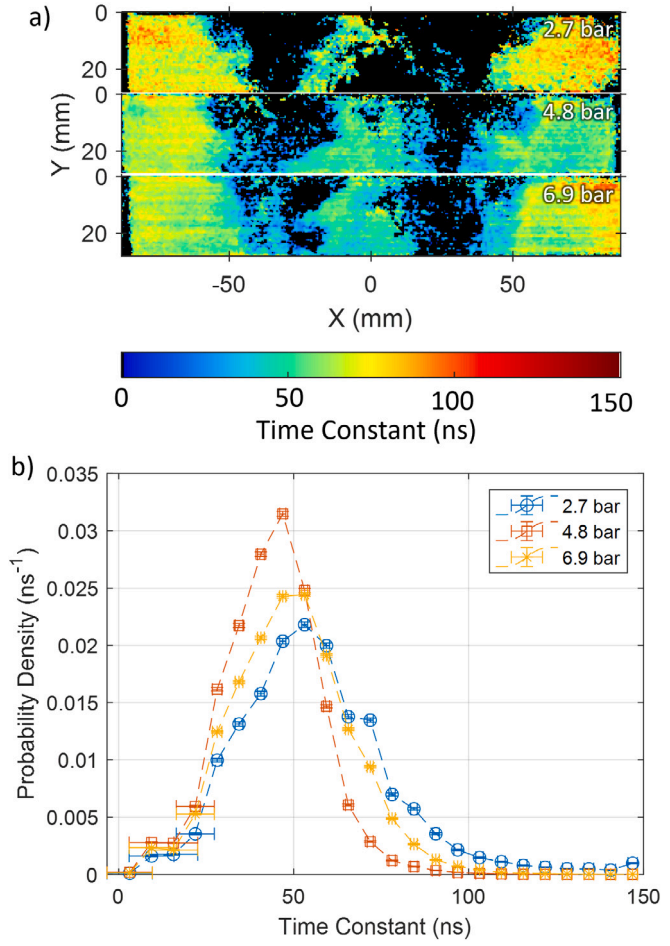

Fig. 10. (a) Time constant distributions are illustrated for 2.74, 4.80, and 6.90 bar conditions with a global equivalence ratio of 0.20. The laser beam passes through the combustor from left to right. Regions with no extractable time decay signal are shown in black. (b) Probability densities of the time constants are illustrated. For these histograms, the vertical error bars indicate the standard deviation of the number of entries in each bin, which is estimated using Poisson statistics. The horizontal error bars represent the standard deviation of the uncertainty due to camera noise and the fitting processes. These are generated using Monte Carlo simulations.

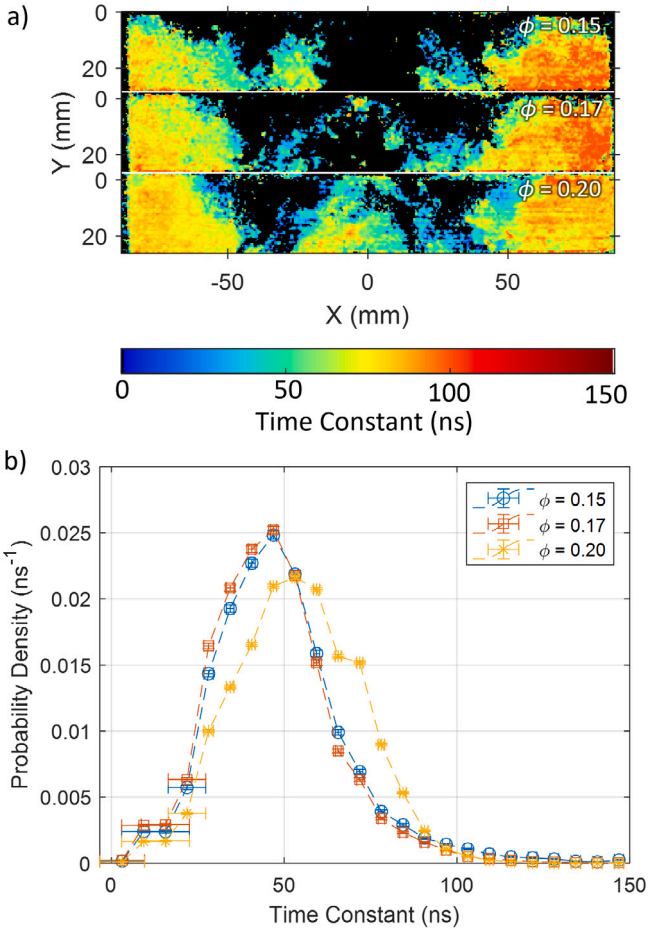

Fig. 11. (a) Time constant distributions are illustrated for global equivalence ratios of 0.15, 0.17 and 0.20 at a constant pressure of 3.4 bar. The laser beam passes through the combustor from left to right. Regions with no extractable time decay signal are shown in black. (b) Probability densities of the time constants are illustrated. For these histograms, the vertical error bars indicate the standard deviation of the number of entries in each bin, which is estimated using Poisson statistics. The horizontal error bars represent the standard deviation of the uncertainty due to camera noise and the fitting processes. These are generated using Monte Carlo simulations.

different decay time. One interesting thing to note is that time constants produced from 55 ns camera integration times with 100 ns sampling intervals are identical to time constants calculated from continuous measurements. Thus, time-constant data taken with the single-camera single-laser shot technique can be readily compared with photodiode or photomultiplier tube data.

Due to the relatively high intensity of the prompt LII signal and the low camera noise, the time constant fits tend to be good quality, especially for time constants that are 30 ns or longer. Shorter time constants, however, contain more uncertainty due to camera noise and the lack of time resolution from the 10 MHz camera acquisition. To estimate the added uncertainty from the temporal resolution, camera noise, and the data fitting process, Monte Carlo simulations of the data are first generated. Then, time constant fits are added and the uncertainty is evaluated. These simulations clearly show that the uncertainties are approximately 1 ns for longer time constants >30 ns and can be as high as 7 ns for shorter time constants.

After time constants are fit to the experimental data, the incandescence decay time distributions are analyzed. Fig. 10a shows time constant fits for 2.7, 4.8, and 6.9 bar absolute (40, 70, and 100 psia) cases at a global equivalence ratio of 0.20, while Fig. 10b shows probability distributions of the time constant near the center injector. For these experiments, the 2.7 bar case appears to have more pixels with longer time constants above 60 ns than the 4.8 and 6.9 bar cases. Otherwise, there is no clear trend in time constants as a function of pressure. For a rough comparison, each time constant distribution can be multiplied by the pressure value to generate a quick approximation of relative soot particle and agglomerate sizes (see Eq. (10)). For this approximation, results appear to indicate that the soot particle sizes increase with pressure for the region of interest. This effect, however, does not match data from prior work [31], where there is little to no change in soot particle size with pressure. One of the potential confounding factors is the contribution of other terms in the TiRe-LII model, which may alter the overall time constant scaling. Other effects like poor droplet breakup, lower signal intensities from lower volume fractions, and weaker recirculation regions (as illustrated in Fig. 7) can also contribute to the measured effect. To understand the true contribution of pressure on particle sizes for this combustor, additional validation via soot sampling is needed.

Fig. 11 shows similar plots for a fixed pressure of 3.4 bar (50 psia) with varying global equivalence ratios of 0.15, 0.17, and 0.20. While the quantity of soot near the center injector does increase with the equivalence ratio, there is no clear trend in the probability distribution of the incandescence time constants for this region. Thus, it appears that more soot is being produced at higher global equivalence ratios,

but the distribution of incandescence decay times and inferred soot particle and agglomerate sizes does not change significantly. This observation matches data from another prior study that shows no clear trend in decay time constant or particle size with equivalence ratio [31]. Across the pressure and equivalence ratio sweeps, the data appears to show that the incandescence decay times do not change significantly over the tested range of pressures and equivalence ratios. Overall, trends relating relative soot particle and agglomerate size to pressure require additional validation.

5. Conclusions

In this work, laser-induced incandescence techniques are used to measure soot volume fractions and soot incandescence decay times in the rich-burn region of a three-injector RQL combustor at various pressures and equivalence ratios. Results show that pressure does not appear to have significant effect on soot concentration at lower equivalence ratios. As pressures increase, however, soot volume fraction become more sensitive to changes in global equivalence ratio, producing significantly more soot at higher ϕ. This effect may be attributed to a combination of increased concentrations of soot in recirculation zones and acceleration of combustion dynamics and soot formation processes in the rich-burn region of the flame at higher pressures. Similar effects have also been noted in the literature, where a power law relationship $f_v = C_0 p_g^n$ is noted between soot volume fraction f_v and ambient pressure [50,51]. This power law relationship can potentially be tested in this combustor in future campaigns for a larger range of pressures.

For the soot incandescence decay time distributions, different trends are noted in the data. For the data gathered in this work, there does not appear to be a measurable dependence of soot incandescence decay times on the pressure or global equivalence ratio. These effects can be compared with conclusions from other work [31], which shows a small amount of time constant dependence on pressure in line with Eq. (10). However, when converted to soot particle sizes using a TiRe-LII model, results in [31] show that the soot particle sizes do not vary for tested pressure range. Additionally, no variations in decay times or calculated soot particle sizes are noted in that previous study as a function of equivalence ratio.

Overall, this work is the first to demonstrate the simultaneous use of LII for soot volume fraction measurement and TiRe-LII for soot incandescence decay time estimates inside a practical multi-sector RQL combustor using realistic swirl injectors and Jet A fuel. Different pressure and equivalence ratios are tested, enabling the study of soot production at various conditions. While several trends are measured in this study, there are still many other parameters and conditions that could be investigated in the future. Variations in injector designs, locations in the flame (such as the quench region of the flame), and fuel types (such as sustainable aviation fuels) can be examined using this facility and suite of diagnostics. Higher pressure, temperature, and global equivalence ratios could also be tested after implementing facilities improvements. Measurements using higher rate framing cameras and complementary diagnostics like chemiluminescence, OH planar laser-induced fluorescence (PLIF), CH_2O PLIF, fuel PLIF, particle image velocimetry, and fuel droplet characterization via phase Doppler particle analysis or digital holography can also be applied to better understand the soot production and oxidation dynamics in these flames. Finally, the laser diagnostics discussed in this work can also potentially be applied in other next-generation combustor topologies to help understand soot production and improve system design for soot reduction.

CRediT authorship contribution statement

Russell McGrath: Data curation, Investigation, Methodology, Software, Visualization, Writing – original draft, Writing – review & editing.

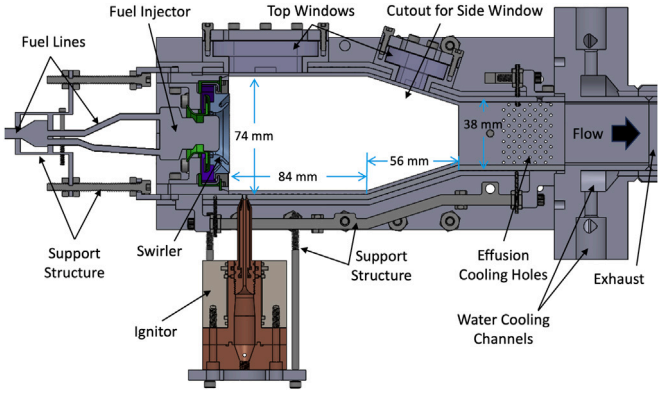

Fig. A.1. Dimensions for the RQL combustor cross section and locations of support structures, fuel lines, and other features are shown.

Jeremiah Juergensmeyer: Data curation, Investigation, Methodology, Visualization. **Robert Bond:** Investigation, Methodology. **Ezekiel Bugay:** Investigation, Methodology, Visualization. **Shawn Wehe:** Investigation, Supervision. **David Wu:** Investigation, Supervision. **Adam Steinberg:** Conceptualization, Funding acquisition, Resources, Supervision. **Wenting Sun:** Conceptualization, Funding acquisition, Project administration, Resources, Supervision. **Yi Chen Mazumdar:** Conceptualization, Funding acquisition, Methodology, Resources, Supervision, Writing – original draft, Writing – review & editing.

Declaration of competing interest

The authors declare that they have no known competing financial interests or personal relationships that could have appeared to influence the work reported in this paper.

Data availability

Data will be made available on request.

Acknowledgments

The authors would like to thank Fang Xu, Rudy Dudebout, and Dustin Brandt at Honeywell International Inc. for their collaboration on this project and assistance with combustor design. The authors would also like to thank Eric Douglas and Andy Zheng for their assistance with measurements and simulations. This research is funded by the U.S. Federal Aviation Administration Office of Environment and Energy through ASCENT, the FAA Center of Excellence for Alternative Jet Fuels and the Environment, Project 70 through FAA Award Number 13-C-AJFE-GIT-080 under the supervision of Prem Lobo and Bahman Habibzadeh. Any opinions, findings, conclusions or recommendations expressed in this material are those of the authors and do not necessarily reflect the views of the FAA.

Appendix. Detailed dimensions and test conditions

A detailed cross-section of the combustor is illustrated in Fig. A.1. Here, the inner width of the combustor is 228 mm and the inner height of the combustor is 74 mm. The rich-burn region ends at the 8.4 mm diameter quench holes; the first row starts 64 mm downstream from the dome face and the second staggered row is 77 mm downstream from the dome face. The straight portion of the combustor is 84 mm long followed by a 56 mm long tapered section to a final exit height of 38 mm. The combustor also has two 19 mm thick windows at the top. Each of these windows is 165 mm wide with a 9.5 mm thick bezel. The top window closest to the dome face is 50 mm long while the top

Table A.1
Measured test conditions for different pressure and equivalence ratio sweeps are shown. Average deviations from the target values are <3% with the largest difference at 8%. Error indicates the measured standard deviation of the data over the sampling period.

	Vessel pressure (bar)		Global equivalence ratio		Air mass	Fuel mass	Air inlet
	Target	Measured	Target	Measured	flow rate (kg/s)	flow rate (kg/s)	temperature (K)
Pressure sweep at $\Phi = 0.12$	2.73	2.77 ± 0.01	0.12	0.120 ± 0.003	0.487 ± 0.001	0.0040 ± 0.0001	575 ± 4
	3.42	3.41 ± 0.00	0.12	0.120 ± 0.001	0.595 ± 0.002	0.0049 ± 0.0000	502 ± 4
	4.12	4.35 ± 0.02	0.12	0.121 ± 0.001	0.808 ± 0.003	0.0067 ± 0.0001	617 ± 1
	4.80	4.83 ± 0.01	0.12	0.122 ± 0.002	0.900 ± 0.002	0.0076 ± 0.0001	613 ± 1
	5.50	5.44 ± 0.01	0.12	0.119 ± 0.001	0.997 ± 0.002	0.0082 ± 0.0001	611 ± 1
	6.18	6.12 ± 0.02	0.12	0.120 ± 0.001	1.120 ± 0.002	0.0093 ± 0.0001	611 ± 1
	6.87	6.93 ± 0.07	0.12	0.125 ± 0.011	1.290 ± 0.012	0.0111 ± 0.0009	592 ± 12
Pressure sweep at $\Phi = 0.20$	2.73	2.74 ± 0.02	0.20	0.198 ± 0.009	0.426 ± 0.001	0.0058 ± 0.0003	616 ± 2
	3.42	3.52 ± 0.01	0.20	0.200 ± 0.004	0.556 ± 0.004	0.0077 ± 0.0001	639 ± 3
	4.12	4.10 ± 0.02	0.20	0.199 ± 0.002	0.753 ± 0.005	0.0103 ± 0.0001	606 ± 1
	4.80	4.80 ± 0.01	0.20	0.201 ± 0.002	0.884 ± 0.002	0.0123 ± 0.0001	604 ± 1
	5.50	5.61 ± 0.19	0.20	0.201 ± 0.005	1.040 ± 0.033	0.0143 ± 0.0003	601 ± 2
	6.18	6.38 ± 0.03	0.20	0.201 ± 0.001	1.170 ± 0.002	0.0161 ± 0.0001	582 ± 10
	6.87	6.90 ± 0.12	0.20	0.210 ± 0.007	1.240 ± 0.020	0.0180 ± 0.0006	561 ± 15
Φ Sweep at 2.7 bar	2.73	2.77 ± 0.01	0.10	0.098 ± 0.004	0.512 ± 0.002	0.0035 ± 0.0001	551 ± 6
	2.73	2.77 ± 0.01	0.12	0.120 ± 0.003	0.487 ± 0.001	0.0040 ± 0.0001	575 ± 4
	2.73	2.77 ± 0.01	0.15	0.150 ± 0.002	0.463 ± 0.001	0.0048 ± 0.0001	595 ± 2
	2.73	2.68 ± 0.01	0.17	0.170 ± 0.002	0.433 ± 0.002	0.0051 ± 0.0001	605 ± 1
	2.73	2.74 ± 0.02	0.20	0.198 ± 0.009	0.426 ± 0.001	0.0058 ± 0.0003	616 ± 2
Φ Sweep at 3.4 bar	3.42	3.43 ± 0.01	0.10	0.097 ± 0.001	0.629 ± 0.003	0.0042 ± 0.0000	604 ± 19
	3.42	3.41 ± 0.00	0.12	0.120 ± 0.001	0.595 ± 0.002	0.0049 ± 0.0000	502 ± 4
	3.42	3.50 ± 0.01	0.15	0.149 ± 0.003	0.584 ± 0.001	0.0060 ± 0.0001	489 ± 3
	3.42	3.45 ± 0.01	0.17	0.170 ± 0.002	0.563 ± 0.004	0.0066 ± 0.0001	474 ± 9
	3.42	3.52 ± 0.01	0.20	0.200 ± 0.004	0.556 ± 0.004	0.0077 ± 0.0001	639 ± 3
Φ Sweep at 6.8 bar	6.87	6.82 ± 0.15	0.10	0.092 ± 0.002	1.310 ± 0.010	0.0084 ± 0.0002	489 ± 16
	6.87	7.08 ± 0.06	0.12	0.122 ± 0.005	1.260 ± 0.016	0.0106 ± 0.0005	563 ± 14
	6.87	7.05 ± 0.03	0.15	0.154 ± 0.002	1.250 ± 0.005	0.0132 ± 0.0001	575 ± 8
	6.87	6.90 ± 0.12	0.20	0.210 ± 0.007	1.240 ± 0.020	0.0180 ± 0.0006	561 ± 15

window further downstream is 25 mm long. Due to viewing angles, the visible width of the combustor centerline is 176 mm from the top windows. Finally, the combustor has two rectangular side windows that are 6.4 mm thick with a height of 94 mm and a length of 164 mm. These windows are slightly oversized and enable views of the rich-burn, quick-mix, and lean-burn regions.

Effusion cooling holes (1.2 mm diameter, 3.5 mm apart with 4.6 mm spacing in staggered rows) are 3D printed at an angle of 20° from horizontal so that air enters the combustor from the pressure vessel to cool the walls and prevent soot collection. Due to the location of the windows and quench holes, some effusion cooling holes are omitted. Each side window also has dedicated holes to provide additional cooling and to prevent soot accumulation (1 mm diameter, 14 along the side nearest the dome face, 28 along the top, 28 along the bottom).

The air splits for the combustor are 18% from the dome face, 44% from the two rows of quench holes, 7% from effusion cooling holes in the rich-burn region, 12% from the holes used for side window cooling, and 19% for the effusion cooling holes in the lean-burn, taper, and exhaust regions. The air that enters the combustor from the dome face is used to drive combustion and control the local equivalence ratio in the rich-burn region. The air that enters from the large quench holes also does a good job penetrating the flow to create the lean-burn region, as illustrated in Fig. 1. The air from effusion and window cooling holes sticks to the walls and windows and does not penetrate the flame.

Using this combustor design, experiments varying pressure and global equivalence ratios can be tested. A table of conditions used for different pressure and equivalence ratio sweeps discussed in this paper is shown in Table A.1. Here, the target and measured pressure (in bar absolute) and global equivalence ratios are shown along with the corresponding air inlet temperature, air mass flow rate, and fuel mass flow rates. Air inlet temperatures are controlled by the building heater air supply and the vessel preheating process. Mass flow rates are controlled using different choke plates placed at the exit of the combustor. Thus, reaching a desired vessel pressure or global equivalence ratio required iteratively adjusting values. Average differences between the target and measured pressure and global equivalence ratio conditions are <3% and the maximum difference between the target and measured values is found to be 8%.

References

[1] Bond TC, Doherty SJ, Fahey DW, Forster PM, Berntsen T, DeAngelo BJ, Flanner MG, Ghan S, Kärcher B, Koch D, Kinne S, Kondo Y, Quinn PK, Sarofim MC, Schultz MG, Schulz M, Venkataraman C, Zhang H, Zhang S, Bellouin N, Guttikunda SK, Hopke PK, Jacobson MZ, Kaiser JW, Klimont Z, Lohmann U, Schwarz JP, Shindell D, Storelvmo T, Warren SG, Zender CS. Bounding the role of black carbon in the climate system: A scientific assessment. J Geophys Res Atmos 2013;118:5380–552. http://dx.doi.org/10.1002/jgrd.50171.

[2] Lighty JS, Veranth JM, Sarofim AF. Combustion aerosols: factors governing their size and composition and implications to human health. J Air Waste Manage Assoc 2000;50(9):1565–618. http://dx.doi.org/10.1080/10473289.2000.10464197.

[3] Mosier SA, Pierce RM. Advanced combustion systems for stationary gas turbine engines Volume I: Review and preliminary evaluation. Report, EPA-600/7-80-017a, U.S. Environmental Protection Agency Interagency Energy/Environment R&D Program; 1980, https://nepis.epa.gov/Exe/ZyPURL.cgi?Dockey=9100BQQR.txt.

[4] Samuelsen S. 3.2.1.3 Rich burn, quick-mix, lean burn (RQL) Combustor. In: The gas turbine handbook. Morgantown, WV, USA: U.S. Department of Energy; 2006, p. 227–33, https://www.netl.doe.gov/sites/default/files/gas-turbine-handbook/3-2-1-3.pdf.

[5] Wang Y, Chung SH. Soot formation in laminar counterflow flames. Prog Energy Combust Sci 2019;74:152–238. http://dx.doi.org/10.1016/j.pecs.2019.05.003.

[6] Gleason K, Carbone F, Gomez A. Pressure and temperature dependence of soot in highly controlled counterflow ethylene diffusion flames. Proc Combust Inst 2019;37(2):2057–64. http://dx.doi.org/10.1016/j.proci.2018.06.156.

[7] Bouvier M, Yon J, Liu F, Cabot G, Grisch F. Application of planar auto-compensating laser-induced incandescence to low-sooting turbulent flames and investigation of the detection gate width effect. Aerosol Sci Technol 2021;55(11):1215–29. http://dx.doi.org/10.1080/02786826.2021.1935699.

[8] Chen Y, Cenker E, Richardson DR, Kearney SP, Halls BR, Skeen SA, Shaddix CR, Guildenbecher DR. Single-camera, single-shot, time-resolved laser-induced incandescence decay imaging. Opt Lett 2018;43(21):5363–6. http://dx.doi.org/10.1364/OL.43.005363.

[9] Wang H. 16.6 Particulate formation and analysis. In: Chemical and combustion kinetics. CRC handbook of shock waves, vol. 3, Academic Press; 2001, p. 257–308. http://dx.doi.org/10.1016/B978-012086430-0/50042-7.

[10] Desgroux P, Faccinetto A, Mercier X, Mouton T, Karkar DA, Bakali AE. Comparative study of the soot formation process in a 'nucleation' and a 'sooting' low pressure premixed methane flame. Combust Flame 2017;184:153–66. http://dx.doi.org/10.1016/j.combustflame.2017.05.034.
[11] Karataş AE, Gülder ÖL. Soot formation in high pressure laminar diffusion flames. Prog Energy Combust Sci 2012;38:818–45. http://dx.doi.org/10.1016/j.pecs.2012.04.00.
[12] Franzelli B, Roussillo M, Scouflaire P, Bonnety J, Jalain R, Dormieux T, Candel S, Legros G. Multi-diagnostic soot measurements in a laminar diffusion flame to assess the ISF database consistency. Proc Combust Inst 2019;37(2):1355–63. http://dx.doi.org/10.1016/j.proci.2018.05.062.
[13] Zhang T, Zhao L, Kholghy MR, Thion S, Thompson MJ. Detailed investigation of soot formation from jet fuel in a diffusion flame with comprehensive and hybrid chemical mechanisms. Proc Combust Inst 2019;37(2):2037–45. http://dx.doi.org/10.1016/j.proci.2018.06.012.
[14] Zhang Y, Liu F, Clavel D, Smallwood GJ, Lou C. Measurement of soot volume fraction and primary particle diameter in oxygen enriched ethylene diffusion flames using the laser-induced incandescence technique. Energy 2019;177:421–32. http://dx.doi.org/10.1016/j.energy.2019.04.062.
[15] Haynes BS, Wagner HG. Soot formation. Prog Energy Combust Sci 1981;7:229–73. http://dx.doi.org/10.1016/0360-1285(81)90001-0.
[16] Wang H. Formation of nascent soot and other condensed-phase materials in flames. Proc Combust Inst 2011;33(1):41–67. http://dx.doi.org/10.1016/j.proci.2010.09.009.
[17] Shaddix CR, Williams TC. The effect of oxygen enrichment on soot formation and thermal radiation in turbulent, non-premixed methane flames. Proc Combust Inst 2017;36(3):4051–9. http://dx.doi.org/10.1016/j.proci.2016.06.106.
[18] Frenklach M, Wang H. Detailed modeling of soot particle nucleation and growth. Symp (Int) Combust 1991;23(1):1559–66. http://dx.doi.org/10.1016/S0082-0784(06)80426-1.
[19] Frenklach M. Reaction mechanism of soot formation in flames. Phys Chem Chem Phys 2002;4(11):2028–37. http://dx.doi.org/10.1039/B110045A.
[20] Wang L, Bauer CK, Gülder ÖL. Soot and flow field in turbulent swirl-stabilized spray flames of Jet A-1 in a model combustor. Proc Combust Inst 2019;37(4):5437–44. http://dx.doi.org/10.1016/j.proci.2018.05.093.
[21] Geigle KP, Zerbs J, Hadef R, Guin C. Laser-induced incandescence for soot measurements in an aero-engine combustor at pressures up to 20 bar. Appl Phys B 2019;125(6):96. http://dx.doi.org/10.1007/s00340-019-7211-2.
[22] Geigle KP, Hadef R, Meier W. Soot formation and flame characterization of an aero-engine model combustor burning ethylene at elevated pressure. In: ASME turbo expo 2013: Turbomachinery technical conference and exposition. 2013, http://dx.doi.org/10.1115/GT2013-95316, V01BT04A024.
[23] Wang L, Chatterjee S, An Q, Steinberg AM, Gülder ÖL. Soot formation and flame structure in swirl-stabilized turbulent non-premixed methane combustion. Combust Flame 2019;209:303–12. http://dx.doi.org/10.1016/j.combustflame.2019.07.033.
[24] Soworka T, Behrendt T, Hassa C, Heinze J, Magens E, Schroll M, di Mare F, Ballantyne S, Gregory J. Experimental investigation of a RQL burner with jet in cross flow fuel injection: Characterization of the reacting flow field at realistic operating conditions. In: ASME turbo expo 2019: Turbomachinery technical conference and exposition. 2019, p. GT2019–91244. http://dx.doi.org/10.1115/GT2019-91244, V04BT04A016.
[25] Meier U, Heinze J, Magens E, Schroll M, Hassa C, Bake S, Doerr T. Optically accessible multisector combustor: Application and challenges of laser techniques at realistic operating conditions. In: ASME turbo expo 2015: Turbomachinery technical conference and exposition. 2015, http://dx.doi.org/10.1115/GT2015-43391, V006T05A022.
[26] Zheng AX, Manikandan SR, Wonfor SE, Steinberg AM, Mazumdar YC. Planar time-resolved laser-induced incandescence for particulate emissions in premixed flames at elevated pressures. In: AIAA SciTech forum. 2023, p. AIAA 2023–2435. http://dx.doi.org/10.2514/6.2023-2435.
[27] Passarelli ML, Wonfor SE, Zheng AX, Manikandan SR, Mazumdar YC, Seitzman JM, Steinberg AM, Bower H, Hong J, Venkatesan K, Benjamin M. Experimental characterization of a lean pre-vaporized premixed combustor for supersonic transport applications. In: AIAA SciTech forum. 2022, p. AIAA 2022–2347. http://dx.doi.org/10.2514/6.2022-2347.
[28] Passarelli ML, Wonfor SE, Zheng AX, Mazumdar YC, Seitzman JM, Steinberg AM, Salazar V, Venkatesan K, Benjamin M. Forced and unforced dynamics of a lean premixed prevaporized combustor for civil supersonic transport. In: AIAA SciTech forum. 2023, p. AIAA 2022–2347. http://dx.doi.org/10.2514/6.2023-0920.
[29] Kuroda R, Tochigi Y, Miyauchi K, Takeda T, Sugo H, Shao F, Sugawa S. A 20Mfps global shutter CMOS image sensor with improved light sensitivity and power consumption performances. ITE Trans Media Technol Appl 2016;4(2):149–54. http://dx.doi.org/10.3169/mta.4.149.
[30] Michael JB, Venkateswaran P, Shaddix CR, Meyer TR. Effects of repetitive pulsing on multi-kHz planar laser-induced incandescence imaging in laminar and turbulent flames. Appl Opt 2015;24(15):3331–44. http://dx.doi.org/10.1364/AO.54.003331.
[31] Zheng AX, Manikandan SR, Wonfor SE, Steinberg AM, Mazumdar YC. Planar time-resolved laser-induced incandescence for pressurized premixed Jet-A combustion. Appl Phys B 2023;129:71. http://dx.doi.org/10.1007/s00340-023-08015-w.
[32] McGrath R, Bugay EM, Juergensmeyer J, Zheng AX, Wu D, Steinberg A, Sun W, Mazumdar YC. Single-camera time-resolved laser-induced incandescence measurements in a RQL aeroengine combustor. In: 13th United States national combustion meeting. USNCM, Sub topic: Diagnostics, 2023, p. 22–31.
[33] Schulz C, Kock BF, Hofmann M, Michelsen H, Will S, Bougie B, Suntz R, Smallwood G. Laser-induced incandescence: Recent trends and current questions. Appl Phys B 2006;83(3):333–54. http://dx.doi.org/10.1007/s00340-006-2260-8.
[34] Snelling DR, Liu F, Smallwood GJ, Gülder ÖL. Determination of the soot absorption function and thermal accommodation coefficient using low-fluence LII in a laminar coflow ethylene diffusion flame. Combust Flame 2004;136(1–2):180–90. http://dx.doi.org/10.1016/j.combustflame.2003.09.013.
[35] Köhler M, Geigle KP, Meier W, Crosland BM, Thomson KA, Smallwood GJ. Sooting turbulent jet flame: Characterization and quantitative soot measurements. Appl Phys B 2011;104:409–25. http://dx.doi.org/10.1007/s00340-011-4373-y.
[36] Mulla I, Yon J, Lefévre G, Lecordier B, Honoré D, Cessou A. Determination of soot volume fraction and particle size distribution in turbulent nonpremixed butane and ethylene jet flames through LII, PPS and SMPS measurements. In: Proceedings of the European combustion meeting. 2017, p. 1–6, https://hal.science/hal-02392366/document.
[37] Charalampopoulos TT, Felske JD. Refractive indices of soot particles deduced from in-situ laser light scattering measurements. Combust Flame 1987;68(12):283–94. http://dx.doi.org/10.1016/0010-2180(87)90005-8.
[38] Lang P, Braeuer PAB, Müller MN, Faderl SR, Huber FJT, Bauer FJ, Will S. Determination of the absorption function of laser-heated soot particles from spectrally resolved laser-induced incandescence signals using multiple excitation wavelengths. Appl Phys B 2023;129:147. http://dx.doi.org/10.1007/s00340-023-08080-1.
[39] Guy G, Betrancourt C, Franzelli B. Estimation of soot absorption function via the two separated pulses laser-induced incandescence technique. Appl Phys B 2023;129:127. http://dx.doi.org/10.1007/s00340-023-08049-0.
[40] Zhang Z, Zhou L, He X. Can laser-induced incandescence calibrated by laser extinction method be used for quantitative determination of soot volume fraction in laminar flames? Appl Energy Combust Sci 2023;13:100103. http://dx.doi.org/10.1016/j.jaecs.2022.100103.
[41] Michelsen HA, Liu F, Kock BF, Bladh H, Boiarciuc A, Charwath M, Dreier T, Hadef R, Hofmann M, Reimann J, Will S, Bengtsson PE, Bockhorn H, Foucher F, Geigle KP, Mounaïm-Rousselle C, Schulz C, Stirn R, Tribalet B, Suntz R. Modeling laser-induced incandescence of soot: A summary and comparison of LII models. Appl Phys B 2007;87(3). http://dx.doi.org/10.1007/s00340-007-2619-5.
[42] Will S, Schraml S, Leipertz A. Two-dimensional soot-particle sizing by time-resolved laser-induced incandescence. Opt Lett 1995;20(22):2342–4. http://dx.doi.org/10.1364/OL.20.002342.
[43] Sun ZW, Gu DH, Nathan GJ, Alwahabi ZT, Dally BB. Single-shot, time-resolved planar laser-induced incandescence (TiRe-LII) for soot primary particle sizing in flames. Proc Combust Inst 2015;35(3):3673–80. http://dx.doi.org/10.1016/j.proci.2014.07.066.
[44] Sjöholm J, Wellander R, Bladh H, Richter M, Bengtsson P-E, Alden M, Chartier C, Andersson O, Johansson B. Challenges for in-cylinder high-speed two-dimensional laser-induced incandescence measurements of soot. SAE Int J Engines 2011;4(1):1607–22. http://dx.doi.org/10.4271/2011-01-1280.
[45] Liu F, Smallwood GJ, Snelling DR. Effects of primary particle diameter and aggregate size distribution on the temperature of soot particles heated by pulsed lasers. J Quant Spectrosc Radiat Transfer 2005;93(1–3):301–12. http://dx.doi.org/10.1016/j.jqsrt.2004.08.027.
[46] Maugendre M. Study of soots particles in kerosene and biofuel flames [Ph.D. Thesis], University of Rouen Normandy; 2009, https://theses.hal.science/tel-00925554/document.
[47] Filippov AV, Rosner DE. Energy transfer between an aerosol particle and gas at high temperature ratios in the Knudsen transition regime. Int J Heat Mass Transfer 2000;43(1):127–38. http://dx.doi.org/10.1016/S0017-9310(99)00113-1.
[48] Fuchs NA. On the stationary charge distribution on aerosol particles in a bipolar ionic atmosphere. Pure Appl Geophys 1963;56(1):185–93. http://dx.doi.org/10.1007/BF01993343.
[49] Fuchs NA, Daisley RE, Fuchs M, Davies CN, Straumanis ME. The mechanics of aerosols. Phys Today 1965;18(4):73. http://dx.doi.org/10.1063/1.3047354.
[50] McArragher JS, Tan KJ. Soot formation at high pressures: A literature review. Combust Sci Technol 1972;5(1):257–61. http://dx.doi.org/10.1080/00102207208952530.
[51] Chu H, Qi J, Feng S, Dong W, Hong R, Qiu B, Han W. Soot formation in high-pressure combustion: Status and challenges. Fuel 2023;345:128236. http://dx.doi.org/10.1016/j.fuel.2023.128236.

Technical Report Documentation Page

1. Report No.	2. Government Accession No.	3. Recipient's Catalog No.
j.jaecs.2024.100269		

4. Title and Subtitle	5. Report Date
Planar laser-induced incandescence for the study of soot production in a multi-sector RQL Jet A combustor	April 2024
	6. Performing Organization Code

7. Author(s)	8. Performing Organization Report No.
McGrath, R., Juergensmeyer, J., Bond, R., Bugay, E., Wehe, S., Wu, D., Steinberg, A., Sun, W. and Mazumdar, Y.C.	

9. Performing Organization Name and Address	10. Work Unit No. (TRAIS)
Center of Excellence for: Alternative Jet Fuels and Environment Georgia Institute of Technology, 270 Ferst Dr, Atlanta, 30332, GA, United States	11. Contract or Grant No. 13-C-AJFE-GIT-080

12. Sponsoring Agency Name and Address	13. Type of Report and Period Covered
Federal Aviation Administration Office of Environment and Energy	Journal Article
	14. Sponsoring Agency Code

15. Supplementary Notes

16. Abstract

Understanding the production of non-volatile particulate matter (nvPM), which is composed primarily of soot, is critical not only for reducing emissions but also for improving engine performance. While there has been significant prior work studying the fundamentals of soot formation, there is significantly less work that investigates soot formation with realistic aeroengine geometries, injectors, and fuels in high pressure conditions. In this work, soot production in a three-sector rich-quench-lean (RQL) aeroengine combustor is studied with Jet A fuel. Global equivalence ratios ranging of 0.10 to 0.20 and pressures ranging from 2.7 to 6.9 bar absolute (40 to 100 psia) are tested. In order to characterize in-situ soot production near the fuel injectors, two-dimensional laser-induced incandescence is utilized to estimate single-shot and average soot volume fractions. Time-resolved laser-induced incandescence is then used to create single camera and single laser-shot incandescence decay time images in order to infer how soot particle sizes evolve. Results show a significant increase in soot production at higher global equivalence ratios and higher pressures. Incandescence decay times, however, do not change significantly over the same range of conditions. These measurements can not only help understand soot distributions in practical RQL systems but also help improve future aeroengine combustor designs.

17. Key Words	18. Distribution Statement
Aeroengine combustion, Jet A fuel, Time-resolved laser induced incandescence, Non-volatile particulate matter, Soot volume fraction, Soot incandescence decay time, ASCENT	

19. Security Classif. (of this report)	20. Security Classif. (of this page)	21. No. of Pages	22. Price
Unclassified	Unclassified		